Overview of Aeroacoustic Testing of the High-Lift Common Research Model

David P. Lockard*, Travis L. Turner†, Christopher J. Bahr‡, and Florence V. Hutcheson‡
NASA Langley Research Center, Hampton, VA 23681

This paper presents an overview of the experimental data obtained in a 2020/2021 aeroacoustic test of the high-lift variant of the common research model. The breadth of the aerodynamic and acoustic measurements is highlighted along with some key results. Aerodynamic data were observed to be consistent with previous observations, and the acoustic measurements were repeatable once some background noise and shear layer issues were resolved. The primary purpose of the test was to evaluate the noise reduction potential of slat noise reduction devices, and a slat-gap filler was found to produce substantial noise reduction over a broad frequency range. The gap filler was designed to meet practical implementation considerations at full scale and constructed out of a shape-memory alloy that would allow the slat to be articulated. However, additional structural testing will be required to demonstrate the performance of the gap filler during slat deployment and retraction. Over 3,500 test points were collected during the test, and only a small fraction of the experimental data have been processed in a preliminary manner. Nonetheless, the results presented demonstrate the quality of the dataset and reveal some insights about slat noise.

Nomenclature

AoA	angle of attack
a	speed of sound
f	frequency
C_D	coefficient of drag
C_L	coefficient of lift
C_p	coefficient of pressure
FSS	full-span slat
M	Mach number $= \|\mathbf{V}\|/a$
MLG	main landing gear
PSD	power spectral density (dB/Hz)
PSS	part-span slat
SGF	slat-gap filler
SCF	slat-cove filler
SPL	sound pressure level
$\|\mathbf{V}\|$	magnitude of velocity vector
x, y, z	Cartesian coordinates

Greek:

η	normalized spanwise distance

I. Introduction

Aircraft noise reduction, including that of the airframe, is an important goal of the NASA Advanced Air Transport Technology (AATT) Project, which is supporting a combined experimental and computational effort to better understand and mitigate the sources associated with slat noise. The nonpropulsive (or airframe) sources of aircraft noise include high-lift devices (e.g., the leading-edge slat and trailing-edge flaps) and the aircraft undercarriage. The ranking of these sources is configuration dependent; however, both model-scale tests [1–7] and flyover noise measurements [8] have identified the leading-edge slat as a prominent source of airframe noise during aircraft approach. To further develop airframe noise reduction technology, NASA has constructed a 10%-scale version of the High-Lift Common Research Model (CRM-HL) developed by Lacy and Sclafani [9]. The original cruise configuration NASA CRM is an open geometry that has been widely used in the AIAA Drag Prediction Workshops [10]. The NASA CRM [11] consists of a contemporary supercritical transonic wing with flow-through nacelles and a fuselage that is representative of a widebody commercial transport aircraft. The new

*Aerospace Technologist, Computational AeroSciences Branch, Mail Stop 128, Associate Fellow, AIAA
†Aerospace Technologist, Structural Acoustics Branch, Mail Stop 463, Associate Fellow, AIAA
‡Aerospace Technologist, Aeroacoustics Branch, Mail Stop 461, Associate Fellow, AIAA

CRM-HL is also an open geometry that was used in the AIAA Geometry and Mesh Generation Workshop [12] and the 3rd AIAA High-Lift Prediction Workshop [13].

Two views of the CRM-HL in the NASA Langley Research Center (LaRC) 14- by 22-foot (14x22) Subsonic Tunnel are shown in Fig. 1. The geometry includes inboard and outboard flaps that meet in the center. There are also inboard and outboard slats, but there is a gap between them to accommodate the pylon for a flow-through nacelle. This is referred to as the part-span slat (PSS) configuration, but the nacelle/pylon can be removed and a bridge piece inserted between the slats to form a full-span slat (FSS). In the landing mode, both flap deflections are set to 37° and the slat deflections are 30°. The geometry includes fifteen slat brackets, three flap brackets, and the corresponding flap track fairings. A four-wheeled main landing gear was developed by NASA for the CRM-HL, and the gear can be partially disassembled to remove some of the small-scale parts. The wing semispan of the CRM-HL is 2.938 m (115.68 in), which corresponds to 10% of a large twin-aisle aircraft. The mean aerodynamic chord (MAC) of the CRM-HL wing is equal to 0.7 m (27.58 in) at a span station of 1.19 m (46.88 in).

NASA developed an active flow control version of the CRM-HL [14–16], and both the conventional and flow control semispan models were tested in the 14x22 in 2018. The effectiveness of a combination of sweeping jets and continuous blowing was demonstrated both experimentally [17] and computationally [18]. Koklu reported on flow visualization results [19] and the effectiveness of a nacelle chine [20] at mitigating some premature stall characteristics. The entry also included aeroacoustic measurements using an on-wall microphone array that were compared with simulation results [21]. In 2019, the model was tested in the QinetiQ 5-metre tunnel [22], where the flap angles, gaps and overhangs were adjusted to optimize the stall angle resulting in the definition of new takeoff and landing configurations [23]. The new 2019 landing configuration [22] is a test case in the 4th AIAA CFD High Lift Prediction Workshop (HLPW-4). Furthermore, a CRM-HL Ecosystem is being developed that will consist of multiple models tested in several facilities.

This paper presents a summary of the 2020/2021 experimental results obtained from testing the original baseline landing configuration in the LaRC 14x22 with the tunnel in the open-jet mode. Measurements include over 900 static pressure ports, unsteady pressure transducers, and an out-of-flow microphone array to make acoustic measurements as shown in Fig. 2. In the open-jet configuration, the walls and ceiling are raised, and the floor is replaced with foam-filled baskets to mitigate acoustic reflections. A traversing array of microphones made measurements on the same side of the model as the on-wall array in 2018. Although some measurements were taken with the original "Aero" slat from 2018, most of the test was devoted to an "Acoustic" slat that was built with brackets that have a more realistic curved shape that would allow them to be stowed.

The primary goal of the 2020 14x22 test was to demonstrate the effectiveness of slat noise-reduction concepts such as the slat-cove filler (SCF) [24, 25] and slat-gap filler (SGF) [26] at a technology readiness level near 5, which is higher than previous tests [24, 27]. Slat-cove fillers were previously tested on a trapezoidal-wing model [24] and the 26% 777 STAR model [27], but those treatments were solid metallic parts that were incapable of being stowed. The current CRM-HL test (sometimes referred to as the CRM-QHL, where the Q stands for quiet) focused on deployable slat gap- and cove-fillers that were constructed out of a nickel-titanium shape-memory alloy (SMA) so that the slat could be retracted. However, the CRM-HL slat will not articulate, and other testing and simulations will be used to evaluate additional structural aspects of the designs. Although both the SGF and SCF designs were tested, only the SGF results are presented in this brief summary as the SGF performed considerably better, and the reasons for the lack of performance of the SCF are still under investigation. Furthermore, only a small subset of the data collected during the test have been processed, and even that processing is preliminary. When testing began in 2020, high background noise levels and decorrelation of the acoustic waves traveling across the shear layer resulted in untrustworthy microphone array results. All of the efforts put into the mitigation of the difficulties are beyond the scope of this paper, but a critical means of reducing the background noise was through the application of adhesive-backed felt to exposed perforated plates on the floor and collector. The white surfaces in Fig. 2 are where the felt was applied. The other essential breakthrough came in the form of an improved array deconvolution processing method that is detailed in a companion paper [28] and briefly explained herein.

Computational simulations have been used to support the model development and to aid in the design of the noise-reduction devices. Although several computational fluid dynamics (CFD) codes were employed in the overall effort, the commercial CFD software PowerFLOW® version 5.5b was used to make aeroacoustic predictions of the noise from the CRM-HL. PowerFLOW® was used extensively during the design of the noise reduction technologies applied to the Gulfstream aircraft model tested in the LaRC 14x22 subsonic tunnel [29, 30], and the noise predictions made before the experimental testing compared very well with the measurements. Initial time-accurate simulations [31] of the flow over the CRM-HL in the landing configuration

were completed in 2017 with PowerFLOW,® and the mean flow field was shown to be in reasonable agreement with the steady CFD results [32] from the FUN3D code [33]. The aerodynamic and acoustic data from the 2018 CRM-HL 14x22 test were compared with PowerFLOW® simulations of both a full-span slat and a part-span slat with a nacelle/pylon [21]. The time-averaged surface pressure was in very good agreement with the simulation results, and synthetic microphone array beamform maps and spectra predicted trends similar to the experimental observations.

Detailed comparisons between the current experimental results and those from 2018 as well as the numerical simulations will be presented in future publications after all of the current data has been processed and analyzed. The purpose of the current paper is to present an overview of the different types of 2020 14x22 measurements and to highlight some of the results that substantiate the data quality.

II. Aerodynamic Results

A. Lift and Drag

The lift and drag from the CRM-HL with a PSS are shown in Figs. 3(a) and (b), respectively. The nacelle included a chine, which was shown to alleviate a premature stall [20]. R217 is from the 2018 closed-wall test, and all of the other curves are from the 2020 open-jet experiment. The slat in the 2018 test is called "Aero" and has straight brackets that mount further downstream on the main element. The 2020 "Acoustic" slat has more realistic, curved brackets that mount closer to the leading edge of the main element. The Aero and Acoustic brackets are compared in Fig. 4. The Aero slat was also tested in the current test, although the majority of the pressure transducers on the slat were not connected due to time constraints. Nonetheless, the results in Fig. 3 show that the Aero (R373 and R377) and Acoustic (R154, R158, R329) slats produced nearly identical lift and drag throughout the polar. Furthermore, the difference between the open-jet and closed-wall results is consistent with the trends predicted by the corrections for the two modes of operation. Data repeatability was slightly better for the lift than the drag, and even more scatter was observed in the moments. We suspect that the brush seal at the bottom of the model was scraping against the uneven floor as the model pivoted, and the ever-changing orientation of the brushes resulted in the inconsistencies. In general, the agreement between Mach 0.16, 0.18, and 0.2 was excellent, but some slight differences were observed at Mach 0.12. Testing at Mach 0.2 was limited because the felt that was applied to the collector had a tendency to come loose, slowing productivity. Hence, the "Acoustic" slat results shown are for Mach 0.18, where multiple repeats are available. In comparing the forces between 2018 and 2020, there is a slight inconsistency between the two tests because of the floor seals. In 2018, a labyrinth seal was employed that made the bottom, straight portion (or peniche) of the fuselage nonmetric, i.e., excluded from the balance measurements. Furthermore, the model had to be elevated by 5.7 cm (2.25 in) in 2020 to get the hinge block above the floor so the model could pivot without interference. Hence, the load on the bottom 14.7 cm (5.75 in) of the 2020 model is extra from what was obtained on the CRM-HL previously, so the best way to evaluate the consistency between the wing loading is through the surface pressure distributions, which will be examined in the next section. Figure 3 also includes lift and drag data from optimized slat gap and overhang settings obtained in the 2019 QinetiQ test [22] that produced different stall characteristics. The curves labeled "Optimized" use these slat settings, but the flap angles were not modified as was also done during the QuinetiQ test.

The lift and drag from the CRM-HL with an FSS are shown in Figs. 5(a) and (b), respectively. In general, the curves are similar to those with the PSS except that stall occurs later, and the post-stall behavior has a more consistent trend. For the FSS, both Mach 0.18 and 0.2 data are included and seem to be consistent. Furthermore, the Acoustic slat was installed two times during the test (R1xx vs R3xx in Figs. 3 and 5), and the force data were consistent across the two installations.

B. Time-Averaged Surface Pressure

The surface pressures along selected planar cuts shown in Fig. 6 are compared between the 2018 and 2020 experiments. The spherical symbols represent the static pressure port locations on the model, and the planar cuts are indicated by the black lines on the wing. The cuts were made with the flaps and slats in the stowed position, so a single plane does not cut through all of the ports when those elements are deployed. The parameter η is the spanwise distance normalized by the total semispan length, where $\eta = 0$ is at the centerline of the fuselage.

The pressure distributions for the 2018 and 2020 experiments at Mach 0.2 along the cuts are shown in Figs. 7 and 8, respectively. The agreement is quite good with an angle of attack adjustment of 1.5°, which is in the expected range when comparing closed-wall and open-jet results. There are some slight differences such as the suction on the flap at $\eta = 0.329$ for the PSS, but the overall agreement is good enough to anticipate that the generated noise should be similar. The 2020 results only have half as many pressure ports on the slat and leading edge of the main element. The instrumentation space was needed for the Acoustic slat and wing under slat surface (WUSS) to accommodate sixty-five unsteady pressure transducers. Nonetheless, enough ports remain to ascertain that the two pressure distributions are similar.

C. Unsteady Surface Pressure

Figure 9 shows the locations of the unsteady pressure transducers that functioned during the 2020 CRM-HL test. Fifty of the transducers worked properly on the slat, slat brackets, and WUSS, which is sufficient to yield insight into the streamwise and spanwise correlations of the oscillations in the slat cove region and provide additional validation data for unsteady simulations. In addition, several transducers around the pylon were used to collect data from both the 2018 and 2020 tests. Sample spectra on the pylon, WUSS, and slat are shown in Fig 10.

III. Acoustics: Array Beamforming Results

A. Array Processing

The microphone array being used in the 2020 test was developed for the 14x22 and consists of 97 microphone channels as detailed by Humphreys [34]. A 110-channel on-wall array was employed in 2018, and the current results will provide the opportunity to make a direct comparison between the two techniques. The on-wall array has the advantage of quick installation that only requires a few days, compared with over a month to convert the 14x22 to the open-jet, semianechoic mode. However, the open-jet mode allows the array to traverse between approximately 56° and 130°, where 90° is directly "below" the model (see Fig. 11). Furthermore, the on-wall array has to contend with significant reflections from the wind tunnel walls. Nonetheless, the results from the 2018 test were encouraging, and the initial comparisons with open-jet measurements are provided in a companion paper [28].

One of the difficulties encountered in this test was the blurring of beamforming and deconvolution results due to turbulent decorrelation. Decorrelation occurs when an acoustic wave passes through a medium with index of refraction variations randomized in time and space, in this case induced by turbulence [35, 36] in the shear layer between the model and the array in the tunnel open-jet configuration. This randomization of the propagation path degrades the computed coherence between pairs of sensors in a microphone phased array, leading to a broadening of the array response to a given acoustic source. For unknown reasons, this effect was worse for the CRM-HL acoustic test than for previous aeroacoustic studies in the 14x22. An example beamforming map contaminated by this effect is shown in Fig. 12(a), and the associated DAMAS output [37] is shown in Fig. 12(b). At this relatively high frequency of 31.5 kHz, the spot size should be relatively small in the standard beamform result, but the decorrelation causes extreme smearing. Without any knowledge of this effect, deconvolution techniques fail to improve the beamform maps. Traditional DAMAS and CLEAN [38] fail miserably, and CLEAN-SC [39], with at least some knowledge of the spatial coherence across the array, does slightly better, but not enough to produce reliable results. Numerous processing methods were investigated, but a change to the DAMAS algorithm was developed that accounted for the effect. This modification is documented in the companion paper by Bahr [28] and briefly described here.

The traditional DAMAS algorithm models propagation from an ideal point source to the microphone array, constructs a rank 1 cross-spectral matrix (CSM) for this synthetic measurement, and beamforms on this synthetic CSM to generate a point spread function. This is done for every grid point in a domain of interest to construct a coefficient matrix. This system matrix is used in an iterative solver to estimate what source distribution would generate the observed beamforming output.

The DAMAS algorithm can be modified to correct for decorrelation by incorporating the mutual coherence function (MCF) [40] into the propagation model. The MCF can be measured using a speaker embedded in the CRM-HL wing, and an appropriate turbulence model can be applied to account for grid points far from the speaker location. The beamforming and iterative solver stages of DAMAS remain unchanged. The output of this coherence-corrected form of DAMAS using the beamforming input of Fig. 12(a) is shown in Fig. 12(c).

The summed spectra for both the whole wing and the isolated slat (as illustrated by the red and blue lines in Fig. 12(c)) associated with these DAMAS results are also computed, emphasizing the inability of traditional DAMAS to localize sources within confined summation bounds (Fig. 13(a)), and the associated improvement with coherence correction (13(b)). The correction is most effective at lower frequencies and for upstream to 90° array positions. Nonetheless, the method produces reasonable results up to 40 kHz, which was the target for the testing. All of the spectra are marked as preliminary as the coherence correction involves the agglomeration of many different speaker cases, and a curve-fit across speeds, angles of attack, and array position. This process is still being optimized, and some improvements are expected. Furthermore, other techniques to improve the coherence between the microphones are being explored, and these may be combined with current coherence correction to DAMAS.

B. Spectra and Beamforming Maps

With coherence-corrected DAMAS processing, the acoustic beamforming results are very repeatable. Figure 14 shows very limited spectral variation across multiple test points for both the PSS and FSS. The conditions are Mach 0.16 with an AoA of 8.5°, and the array directly below the model at 90°. Other than the slat tones, centered around 8 kHz, the spectral results are very consistent. Slat tones are common in model scale testing, but they are not of practical interest as they have been found to disappear in higher Reynolds number tests [41]. The PSS and FSS results are quite similar, with the PSS having slightly higher levels because of the additional slat side edges around the pylon. All of the spectra presented in the remainder of the paper were confirmed with at least two test points to have repeatability of similar quality to that observed in Fig. 14. However, repeat points are rarely included hereafter for the sake of clarity.

The DAMAS beamform maps associated with one of the PSS CRM-HL points are presented in Fig. 15, and those for the FSS in Fig. 16. The map at each frequency is shown with a range of 0 to -16 dB relative to the "Max" level given in each subfigure. Hence, to compare maps from different points, the "Max" needs to be taken into account. In general, the inboard slat with the PSS produces the most noise at lower frequencies, whereas the outboard slat tends to be louder for the FSS. Sources around the outboard end of the inboard slat are often dominant with the PSS, and the location of the tone at 8 kHz is in that location. For the FSS, the tone emanates from a position that is further outboard. The tone source location varied with every configuration and flow parameter indicating the particular conditions necessary to produce a resonance are highly dependent on the geometry and flow. Aside from the tones, the slat tips and brackets are often associated with the peak levels in the maps. However, the distributed nature of the slat source means that the peak source may not be the dominant factor in the integrated noise levels. Above 15 kHz in Fig. 15, a source around the intersection of the fuselage and the floor is evident. Later in the test, the bottom 15 cm (6 in) of the fuselage was treated with adhesive-backed felt, and this source disappeared. The FSS result in Fig. 16 was obtained with the felt applied to the bottom 15 cm of the fuselage. We speculate that the horshoe vortex generated at the intersection of the lifting body and the floor interacts with the lower part of the fuselage and generates noise. The strength if this source increased with angle of attack, indicating that it was sensitive to the model lift.

The effect of the Mach number on the noise from the FSS CRM-HL is shown in Fig. 17. Other than the tone, all of the spectral features are relatively insensitive to the flow speed; however, the levels increase approximately with the flow speed to the sixth power. At frequencies below 4 kHz, the scaling appears to be closer to a power of five, and the scaling between 6 and 12 kHz is difficult to ascertain because of the tones.

Figure 18(a) shows that the noise from the CRM-HL increases significantly as the AoA is increased, with the difference between 13° and 8.5° greater than that between 4° and 8.5°. Other than the tones, the spectral shapes for all of the angles of attack are relatively similar. However, the spectral shapes do change as the array is traversed for a fixed set of conditions as illustrated in Fig. 18(b). All of the curves coalesce around 8 kHz, but the levels are otherwise much higher for the downstream positions. These curves have not been corrected for the propagation distance, which increases away from the array position of 90°. Taking that into account would further emphasize the higher levels in the downstream arc relative to 90°.

As previously mentioned, both the Aero and Acoustic slats with their different bracket shapes were tested. In addition, three of the fifteen slat brackets were removed from the Acoustic slat during testing, and inserts in the main that surround the brackets were also removed. Images of these configurations are in Fig. 19 with their spectra presented in Fig. 20(a). In addition, the spectra include those for the Aero slat with and without the optimized slat gap and overhang. The Aero slat has higher levels than the Acoustic slat as well as exhibits two frequency ranges with substantial tonal content. However, the optimized settings with only slightly different rigging eliminated all of the tonal content between 6 and 15 kHz. Outside of this range, the levels are still higher

with the optimized settings. Levels a couple dB lower than that of the baseline Acoustic slat were obtained when brackets 7, 8, and 9 (of 15) were removed. Given the more pronounced brackets on the Aero slat, the variation in levels observed outside of the tones are likely indicating that the brackets are an important noise source. However, attempts to quiet the brackets by wrapping them in foam or applying felt did not change the noise measurably. Nonetheless, numerical simulations of the CRM-HL with and without the slat brackets revealed a similar trend in the noise, so further investigations of the influence of brackets on slat noise may be conducted through simulations.

The effect of inserts around the slat brackets where they enter the main element was also investigated. Figure 20(b) compares the spectra from the baseline with the inserts (Fig. 19(b)) to those when the inserts were removed. Above 3 kHz, except around the tone, the case with the inserts was a couple of decibels quieter. Details about the slat brackets and the inserts appear to have a significant influence on the overall noise from the slat.

A photo of a low-noise slat with a slat-gap filler installed is shown in Fig. 21(a). The SGF can be distinguished by the blueish tint that resulted from the heat treating process. In addition, the image shows smooth transition tips (slat side edges), which could be implemented using continuous moldline technology (CMT), but alternative implementations are also under investigation. The smooth tips are contrasted with a standard tip in Fig. 21(b).

For angles of attack below 13°, the SGF has little effect on the overall lift as Fig. 22(a) shows. Although the total lift is similar to that of the baseline, the distribution across elements is different. The SGF slat was only sparsely instrumented, but did have enough static ports to confirm that closing the slat gap with the SGF causes some of the load on the leading edge of the main element to be shifted onto the slat. For the overall drag, the loads are actually slightly lower with the SGF. Figure 22(b) compares the drag of the baseline and SGF configurations, and the SGF drag was consistently below that of the baseline. Beyond 13°, the SGF configuration would undoubtedly stall earlier than the baseline. However, the SGF is designed to retract quickly should an anomalous, high AoA condition occur, so the performance of the baseline with an open gap would be recovered.

Although the aerodynamic performance of the SGF is important, the whole reason for investigating such a design is to reduce the noise from the slat. As Fig. 23(a) shows, the SGF on the PSS CRM-HL provides a broadband reduction on the order of 5 dB with the standard tips, but the reduction approaches 10 dB with the smooth tips. Furthermore, the case with only smooth inboard tips performed similarly to having all four smooth tips, except at 11 kHz where the outboard smooth tip actually generated more noise. The smooth tip designs were constrained by implementation details, and a small pocket in the tip may have been responsible for the peak at 11 kHz. The beamform maps for the case with the SGF and standard tips are presented in Fig. 24 and those with smooth tips in Fig. 25. With the standard tips, the primary noise sources are at the inboard ends of the slats, but with the smooth tips, the outboard end of the outboard slat has the peak level, although at most frequencies that level is still well below the maximum observed with the standard tips.

To assess the impact of the SGF on the overall airframe noise, cases with the landing gear were investigated. The detailed two-wheeled landing gear shown in Fig. 21(c) was tested with the baseline and SGF slats, as well as a simplified MLG that had the door, side braces, and small-scale parts removed (see Fig. 21(d)). The simple gear is an approximation of a gear quieted with streamlined side braces and either fairings or a design that hides the details around the post. Figure 23(b) compares the spectra from the FSS CRM-HL with and without the MLG and the SGF. The MLG on the baseline slat is about 2 to 5 dB higher than the spectra without the gear. Applying the SGF with the MLG reduces the noise by about 4 to 5 dB, and using the simple gear further reduces the noise another 2 to 3 dB. The case with the SGF but without the MLG is even another 4 to 5 dB quieter, but this would only be relevant before the landing gear is deployed. The beamform maps for the loudest configuration with the MLG and the untreated slat are shown in Fig. 26, and those with the MLG and SGF are in Fig. 27. The MLG is clearly the loudest noise source on the model, but overall influence of the slat on the spectra is still substantial because of the more distributed nature of the slat source. With the SGF in place, the beamform maps rarely indicate anything within 16 dB of the gear source. The flaps on the CRM-HL are fairly quiet, with most of the noise associated with the flap brackets. Removal of the flap track fairings made almost no difference to the noise observed just outboard of each fairing. Nonetheless, on most aircraft, the flaps, slats, and landing gear all produce noise of a similar magnitude, and all must be quieted to obtain substantial system level noise reduction.

IV. Conclusions

Despite numerous testing difficulties, the 2020/2021 aeroacoustic test of the CRM-HL produced a wealth of quality experimental data that are being used to further our understanding of airframe noise and to substantiate

the noise reduction potential of low-noise slats. In particular, the slat-gap filler with smooth tips was found to provide 10 dB of noise reduction from the slat region, and 4-5 dB for the entire wing, including a main landing gear. The data underscore the importance of geometric details as the noise was found to be sensitive to the slat brackets, tips, and even the gap in the main element around the brackets.

Only a small subset of the experimental data has been processed in a preliminary manner using a newly developed coherence-correction method for DAMAS that accounts for significant shear layer induced decorrelation of microphone signals across the array face. Although some further enhancements are likely, the beamform maps and integrated spectra presented all exhibit excellent repeatability and consistent trends. Together with the forces and surface pressure data, the dataset provides an extensive set of measurements of a modern, yet open, wing design. The data for the baseline PSS and FSS CRM-HL are planned to be part of a future Benchmark problems for Airframe Noise Configurations (BANC) workshop [42] to further the development of simulation techniques for predicting airframe noise. A thorough reporting on the aerodynamic and acoustic data and on the treatments and model development are also planned for future AIAA conferences.

Acknowledgment

This work was supported by the NASA Advanced Air Transport Technology (AATT) Project. The authors gratefully acknowledge the hard work of all of the participants in the 2020/2021 NASA LaRC 14x22 test.

References

[1] Hayes, J. A., Horne, W. C., Soderman, P. T., and Bent, P. H., "Airframe Noise Characteristics of a 4.7% Scale DC-10 Model," AIAA Paper 1997-1594, 1997.

[2] Storms, B. L., Ross, J. C., Horne, W. C., Hayes, J. A., Dougherty, R. P., Underbrink, J. R., Scharpf, D. F., and Moriarty, P. J., "An Aeroacoustic Study of an Unswept Wing with a Three-Dimensional High Lift System," NASA TM 112222, February 1998.

[3] Dobrzynski, W., Nagakura, K., Gehlhar, B., and Buschbaum, A., "Airframe Noise Studies on Wings with Deployed High-Lift Devices," AIAA Paper 1998-2337, 1998.

[4] Storms, B. L., Hayes, J. A., Moriarty, P. J., and Ross, J. C., "Aeroacoustic Measurements of Slat Noise on a Three-Dimensional High-Lift System," AIAA Paper 1999-1957, 1999.

[5] Choudhari, M. M., Lockard, D. P., Macaraeg, M. G., Singer, B. A., Streett, C. L., Neubert, G. R., Stoker, R. W., Underbrink, J. R., Berkman, M. E., Khorrami, M. R., and Sadowski, S. S., "Aeroacoustic Experiments in the Langley Low-Turbulence Pressure Tunnel," NASA TM 211432, February 2002.

[6] Mendoza, F., and Brooks, T., "Aeroacoustic Measurements of a Wing/Slat Model," AIAA Paper 2002-2604, 2002.

[7] Terracol, M., Manoha, E., and Lemoin, B., "Noise Sources Generation in a Slat Cove: Hybrid Zonal RANS/LES Simulation and Dedicated Experiment," AIAA Paper 2011-3203, 2011.

[8] Chow, L. C., Mau, K., and Remy, H., "Landing Gears and High Lift Devices Airframe Noise Research," AIAA Paper 2002-2408, 2002.

[9] Lacy, D. S., and Sclafani, A. J., "Development of the High Lift Common Research Model (HL-CRM): A Representative High Lift Configuration for Transonic Transports," AIAA Paper 2016-0308, 2016.

[10] AIAA Drag Prediction Workshop Web Site: https://aiaa-dpw.larc.nasa.gov/, retrieved 20 May, 2021.

[11] NASA Common Research Model Web Site: https://commonresearchmodel.larc.nasa.gov/, retrieved 17 May, 2021.

[12] AIAA Geometry and Mesh Generation Web Site: http://www.gmgworkshop.com/, retrieved 17 May, 2021.

[13] AIAA High Lift Prediction Workshop: https://hiliftpw.larc.nasa.gov/, retrieved 20 May, 2021.

[14] Lin, J. C., Melton, L. G., Hannon, J. A., Andino, M. Y., Koklu, M., Paschal, K. B., and Vatsa, V. N., "Wind Tunnel Testing of Active Flow Control on the High Lift Common Research Model," AIAA Paper 2019-3723, 2019.

[15] Melton, L. G., Lin, J. C., Hannon, J. A., Koklu, M., Andino, M. Y., and Paschal, K. B., "Sweeping Jet Flow Control on the Simplified High-Lift Version of the Common Research Model," AIAA Paper 2019-3726, 2019.

[16] Vatsa, V. N., Duda, B. M., Lin, J. C., Pack, L. G., and O'Connell, M. D., "Comparative Study of Active Flow Control Strategies for Lift Enhancement of a Simplified High-Lift Configuration," AIAA Paper 2019-3724, 2019.

[17] Lin, J. C., Melton, L. G., Hannon, J. A., Andino, M. Y., Koklu, M., Paschal, K. B., and Vatsa, V. N., "Wind Tunnel Testing of High Efficiency Low Power (HELP) Actuation for Active Flow Control," AIAA Paper 2020-0783, 2020.

[18] Vatsa, V. N., Lin, J. C., Pack, L. G., Lockard, D. P., and Ferris, R., "CFD and Experimental Data Comparisons for Conventional and AFC-Enabled CRM High-Lift Configurations," AIAA Paper 2020-2939, 2020.

[19] Koklu, M., Melton, L. G., Lin, J. C., Hannon, J. A., Andino, M. Y., Paschal, K. B., and Vatsa, V. N., "Surface Flow Visualization of the High Lift Common Research Model," AIAA Paper 2019-3727, 2019.

[20] Koklu, M., Lin, J. C., Hannon, J. A., Melton, L. G., Andino, M. Y., Paschal, K. B., and Vatsa, V. N., "Mitigation of Nacelle/Pylon Wake on the High-Lift Common Research Model Using a Nacelle Chine," AIAA Paper 2020-0786, 2020.

[21] Lockard, D. P., O'Connell, M. D., Vatsa, V. N., and Choudhari, M. M., "Assessment of Aeroacoustic Simulations of the High-Lift Common Research Model," AIAA Paper 2019-2460, 2019.

[22] Clark, A. M., Slotnick, J. P., Taylor, N. J., and Rumsey, C. L., "Requirements and Challenges for CFD Validation within the High-Lift Common Research Model Ecosystem," AIAA Paper 2020-2772, 2020.

[23] Lacy, D. M., and Clark, A. M., "Definition of Initial Landing and Takeoff Reference Configurations for the High Lift Common Research Model (CRM-HL)," AIAA Paper 2020-2771, 2020.

[24] Streett, C. L., Casper, J., Lockard, D. P., Khorrami, M. R., Stoker, R., Elkoby, R., Wenneman, W., and Underbrink, J., "Aerodynamic Noise Reduction for High-Lift Devices on a Swept Wing Model," AIAA Paper 2006-0212, 2006.

[25] Scholten, W. D., Hartl, D. J., Turner, T. L., and Kidd, R. T., "Development and Analysis-Driven Optimization of Superelastic Slat-Cove Fillers for Airframe Noise Reduction," *AIAA Journal*, Vol. 54, No. 3, 2016, pp. 1078–1094.

[26] Turner, T. L., and Long, D. L., "Development of a SMA-Based, Slat-Gap Filler for Airframe Noise Reduction," AIAA Paper 2015-0730, 2015.

[27] Horne, W. C., Burnside, N. J., Soderman, P. T., Jaeger, S. M., Reinero, B. R., James, K. D., and Arledge, T. K., "Aeroacoustic Study of a 26%-Scale Semispan Model of a Boeing 777 Wing in the NASA Ames 40- by 80-Foot Wind Tunnel," NASA TP 2004-212802, October 2004.

[28] Bahr, C. J., "Toward Relating Open- and Closed Test Section Microphone Phased Array Aeroacoustic Measurements," to be published at the 2021 AIAA AVIATION Meeting, August 2021.

[29] Fares, E., Casalino, D., and Khorrami, M., "Evaluation of Airframe Noise Reduction Concepts via Simulations Using a Lattice Boltzmann Approach," AIAA Paper 2015-2988, 2015.

[30] Khorrami, M. R., Humphreys, W. M., Lockard, D. P., and Ravetta, P. A., "An Assessment of Flap and Main Landing Gear Noise Abatement Concepts," AIAA Paper 2015-2978, 2015.

[31] Lockard, D. P., Choudhari, M. M., Vatsa, V. N., O'Connell, M. D., Duda, B. M., and Fares, E., "Noise Simulations of the High-Lift Common Research Model," AIAA Paper 2017-3362, 2017.

[32] Rivers, M., Hunter, C., and Vatsa, V., "Computational Fluid Dynamic Analyses for the High-Lift Common Research Model Using the USM3D and FUN3D Flow Solvers," AIAA Paper 2017-0320, 2017.

[33] Biedron, R. T., Derlaga, J. M., Gnoffo, P. A., Hammond, D. P., Jones, W. T., Kleb, B., Lee-Rausch, E. M., Nielsen, E. J., Park, M. A., Rumsey, C. L., Thomas, J. L., , and Wood, W. A., "FUN3D Manual: 12.4," NASA TM 2014-218179, March 2014.

[34] Humphreys, W. M., Brooks, T. F., Bahr, C. J., Spalt, T. B., Bartram, S. M., Culliton, W., and Becker, L., "Development of a Microphone Phased Array Capability for the Langley 14- by 22-foot Subsonic Tunnel," AIAA Paper 2014-2343, 2014.

[35] Dougherty, R. P., "Turbulent Decorrelation of Aeroacoustic Phased Arrays: Lessons from Atmospheric Science and Astronomy," AIAA Paper 2003-3200, 2003.

[36] Ernst, D., Spehr, C., and Berkefeld, T., "Decorrelation of Acoustic Wave Propagation through the Shear Layer in Open Jet Wind Tunnel," 2015-2976, 2015.

[37] Brooks, T., and Humphreys, W. M., "A Deconvolution Approach for the Mapping of Acoustic Sources (DAMAS) Determined from Phased Microphone Arrays," *Journal of Sound and Vibration*, Vol. 294, 2006, pp. 856–879.

[38] Sijtsma, P., and Stoker, R. W., "Determination of Absolute Contributions of Aircraft Noise Components using Fly-Over Array Measurements," AIAA Paper 2004-2958, 2004.

[39] Sijtsma, P., "CLEAN Based on Spatial Source Coherence," AIAA Paper 2007-3436, 2007.

[40] Wilson, D. K., "Performance Bounds for Acoustic Direction-of-Arrival Arrays Operating in Atmospheric Turbulence," *JASA*, Vol. 103, No. 3, 1998, pp. 1306–1319.

[41] Ahlefeldt, T., "Microphone Array Measurement in European Transonic Wind Tunnel at Flight Reynolds Numbers," *AIAA Journal*, Vol. 55, No. 1, 2017, pp. 36–48.

[42] Benchmark problems for Airframe Noise Configurations (BANC) Workshops, URL: https://banc-workshop.larc.nasa.gov/, retrieved 17 May, 2021.

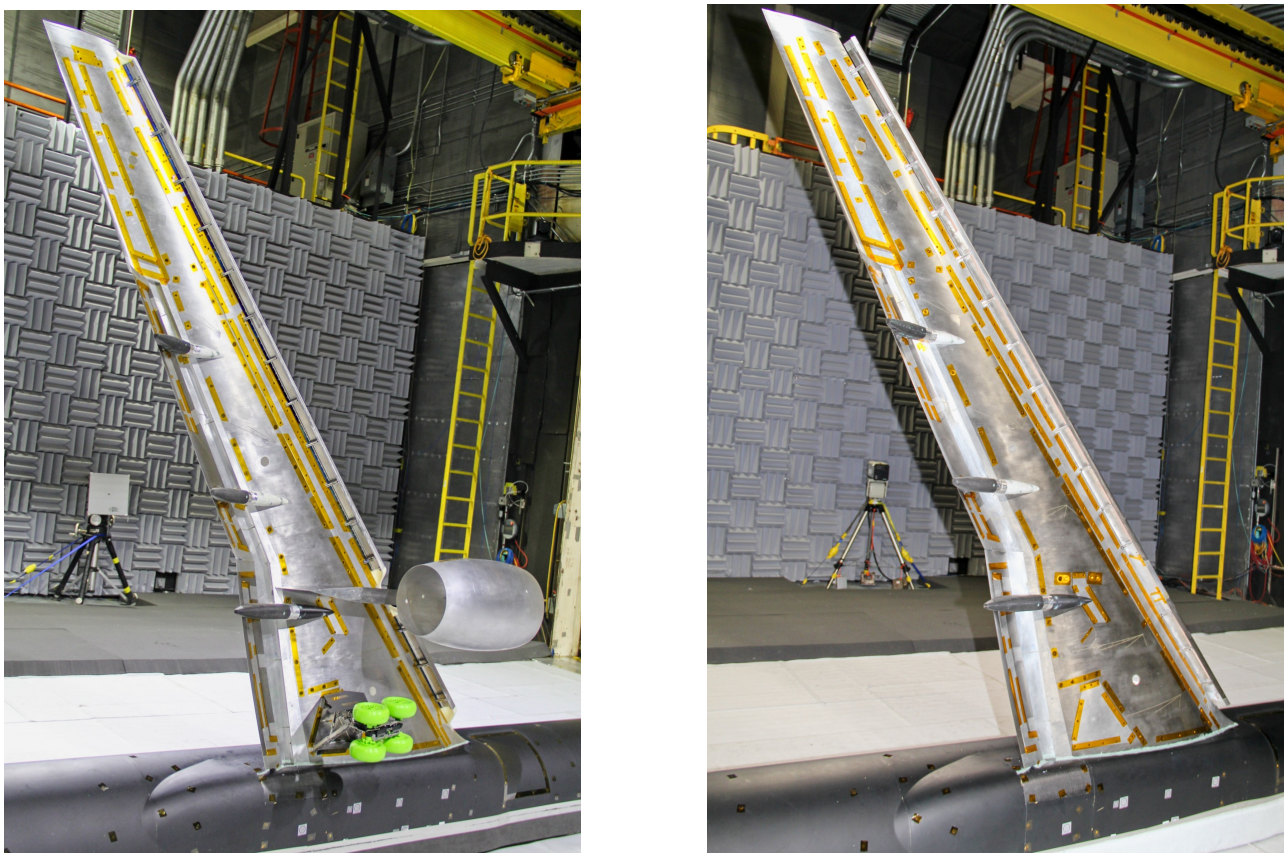

(a) PSS with MLG

(b) FSS

Fig. 1 CRM-HL configurations from the 2021 test in the 14x22 wind tunnel.

Fig. 2 CRM-HL installed in the 14x22 wind tunnel, with microphone array at left.

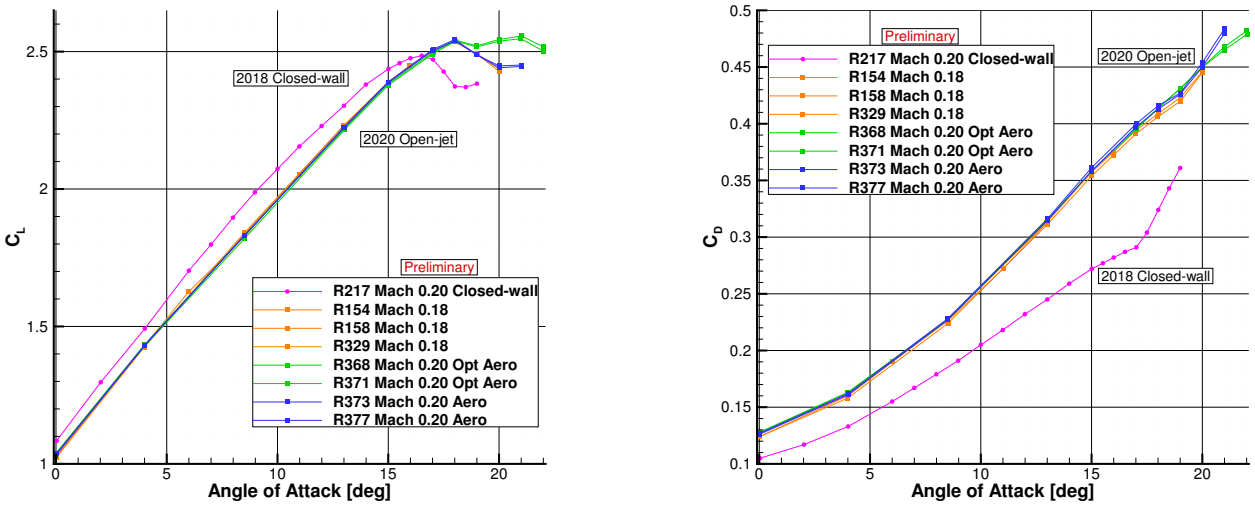

(a) Lift

(b) Drag

Fig. 3 Lift and drag of the CRM-HL with the PSS.

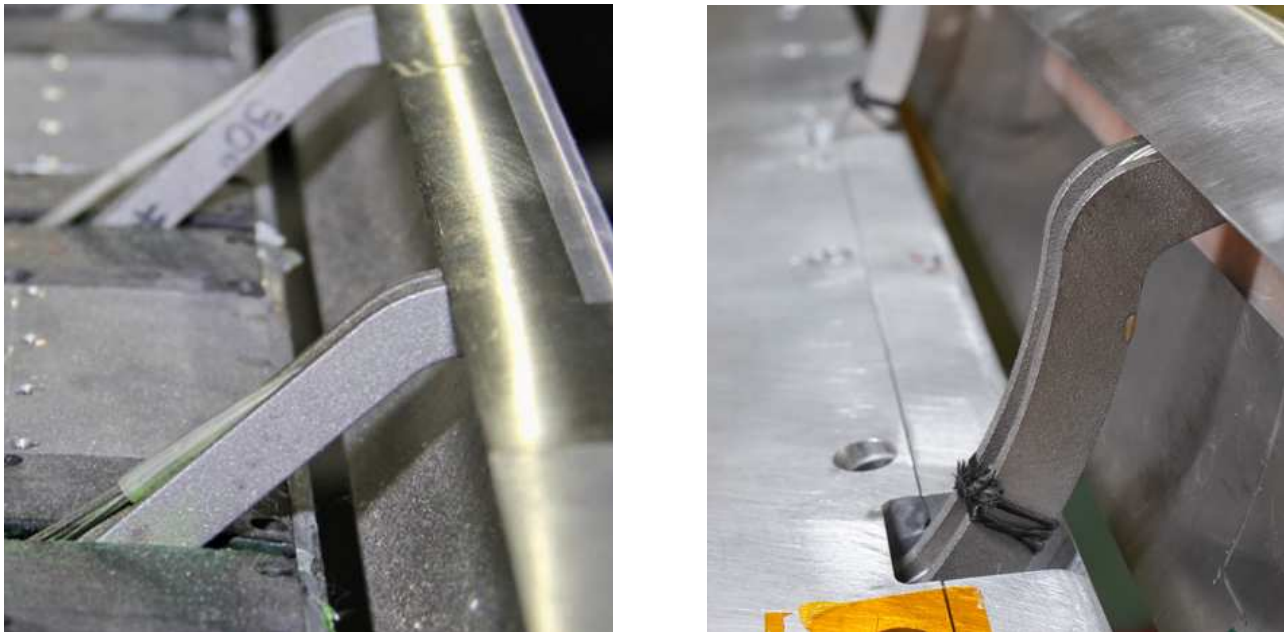

(a) Aero Slat (b) Acoustic Slat

Fig. 4 Images of the slat brackets on the CRM-HL Model.

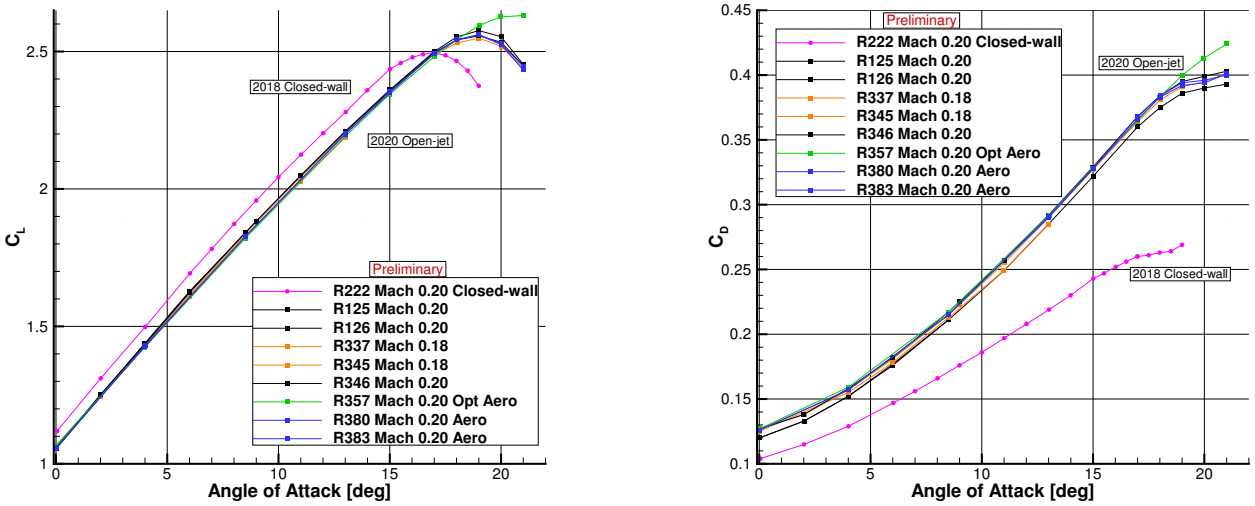

(a) Lift (b) Drag

Fig. 5 Lift and drag of the CRM-HL with the FSS.

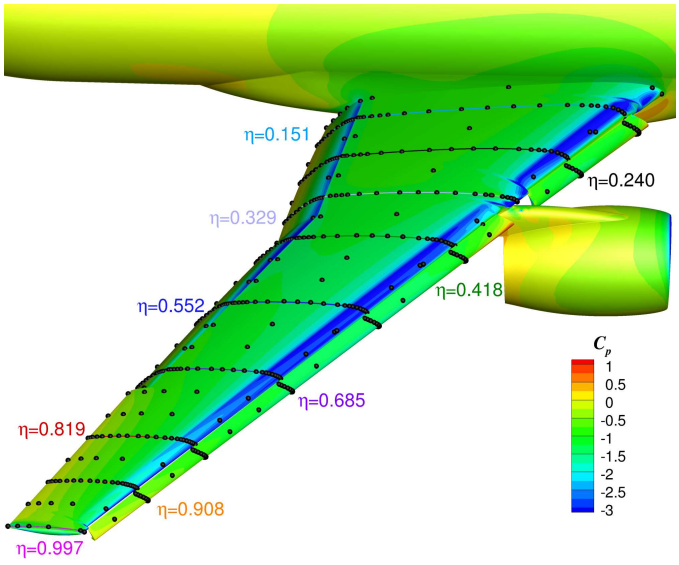

Fig. 6 Planar wing cuts used for comparisons with experimental data. Symbols indicate static pressure port locations. The flap break is at $\eta = 0.37$, and the outboard flap extends to $\eta = 0.72$. The pressure coefficient contour levels were obtained from CFD.

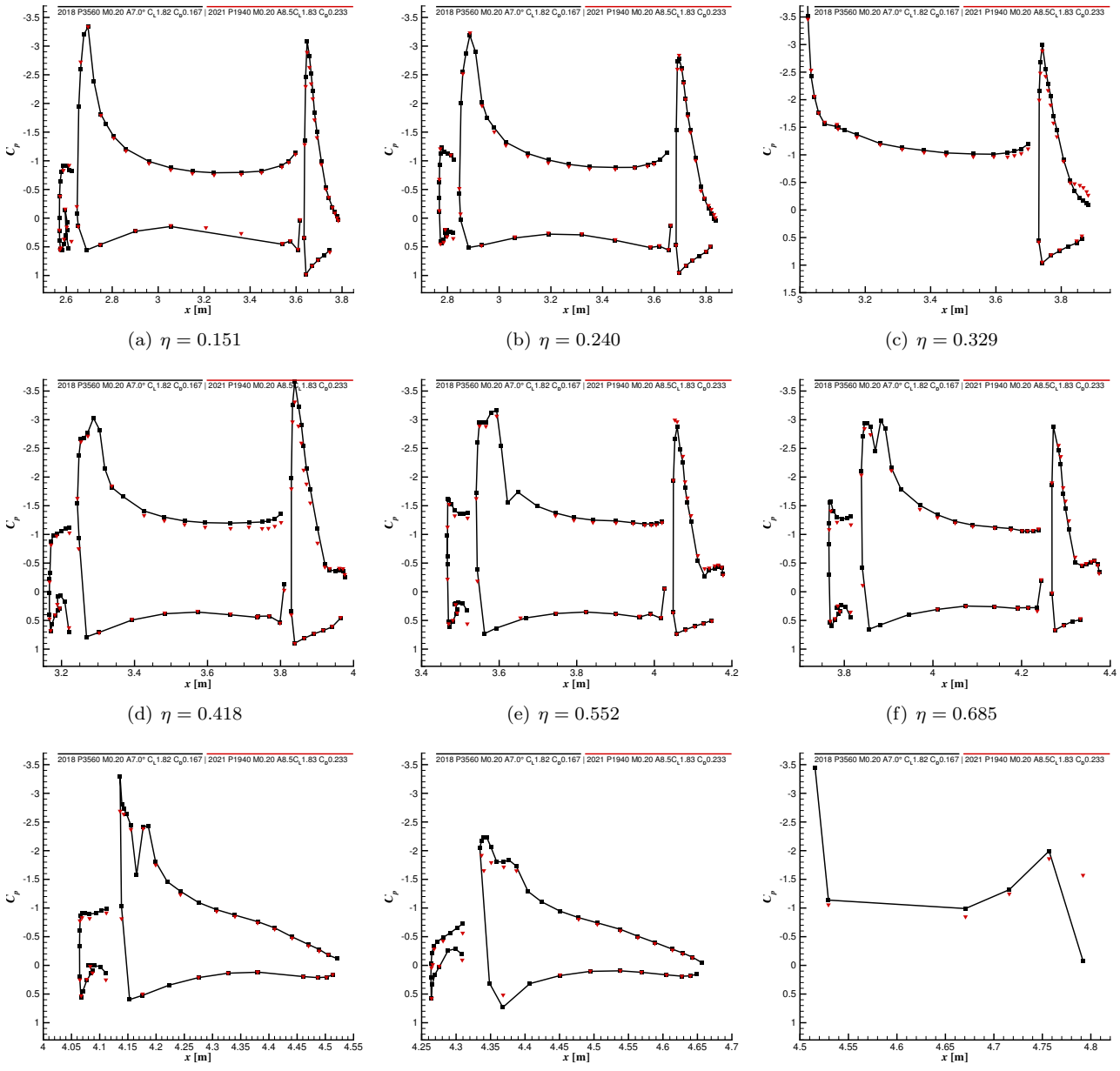

(a) $\eta = 0.151$ (b) $\eta = 0.240$ (c) $\eta = 0.329$

(d) $\eta = 0.418$ (e) $\eta = 0.552$ (f) $\eta = 0.685$

(g) $\eta = 0.819$ (h) $\eta = 0.908$ (i) $\eta = 0.997$

Fig. 7 14x22 experimental surface C_p distributions along cuts through the CRM-HL wing for the baseline PSS configuration at $M = 0.2$; 2018 (closed wall, black lines/squares) at AoA $= 7°$ compared with 2020/2021 (open jet, red triangles) at AoA $= 8.5°$.

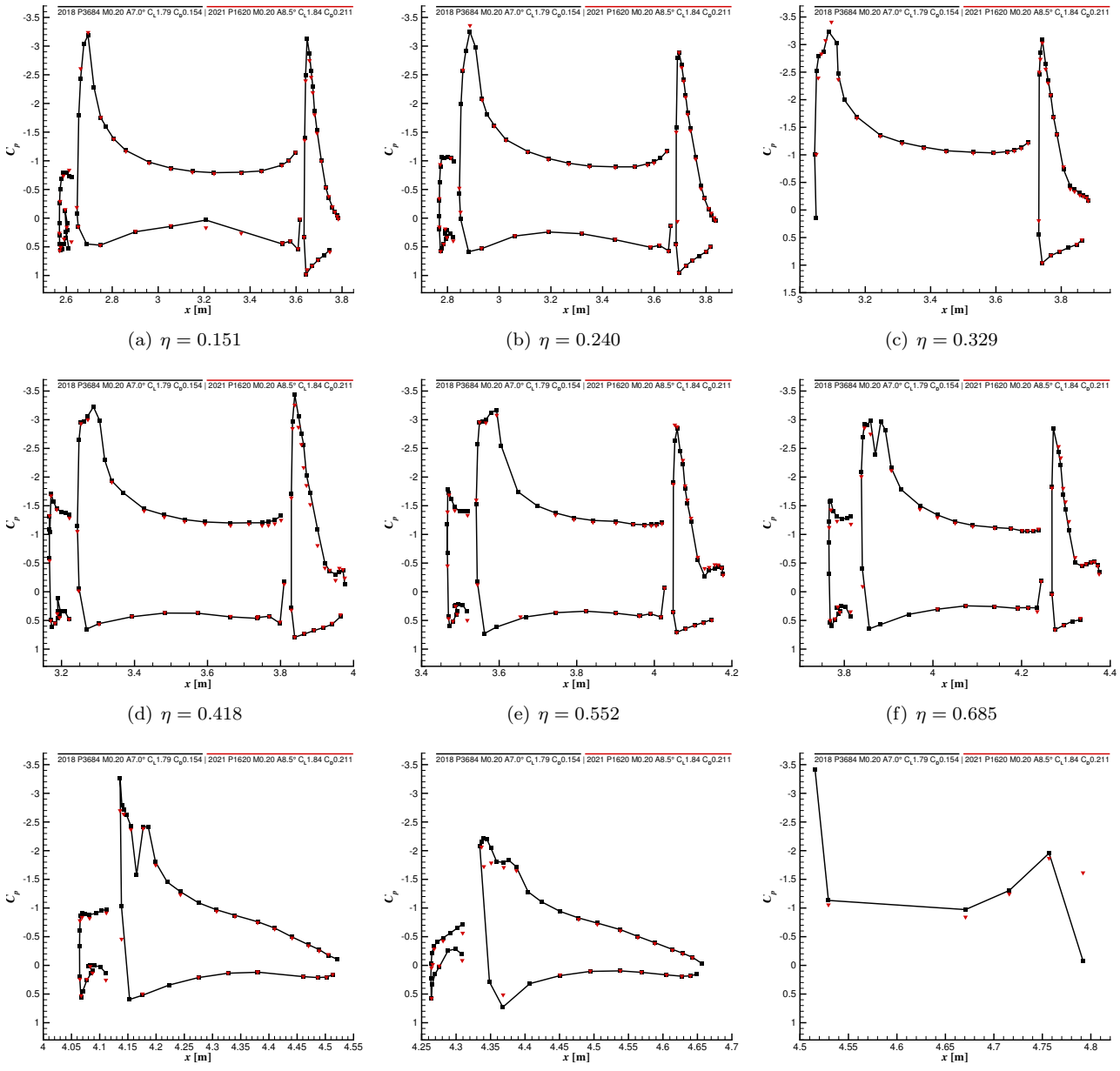

(a) $\eta = 0.151$ (b) $\eta = 0.240$ (c) $\eta = 0.329$

(d) $\eta = 0.418$ (e) $\eta = 0.552$ (f) $\eta = 0.685$

(g) $\eta = 0.819$ (h) $\eta = 0.908$ (i) $\eta = 0.997$

Fig. 8 14x22 experimental surface C_p distributions along cuts through the CRM-HL wing for the baseline FSS configuration at $M = 0.2$; 2018 (closed wall, black lines/squares) at AoA $= 7°$ compared with 2020/2021 (open jet, red triangles) at AoA $= 8.5°$.

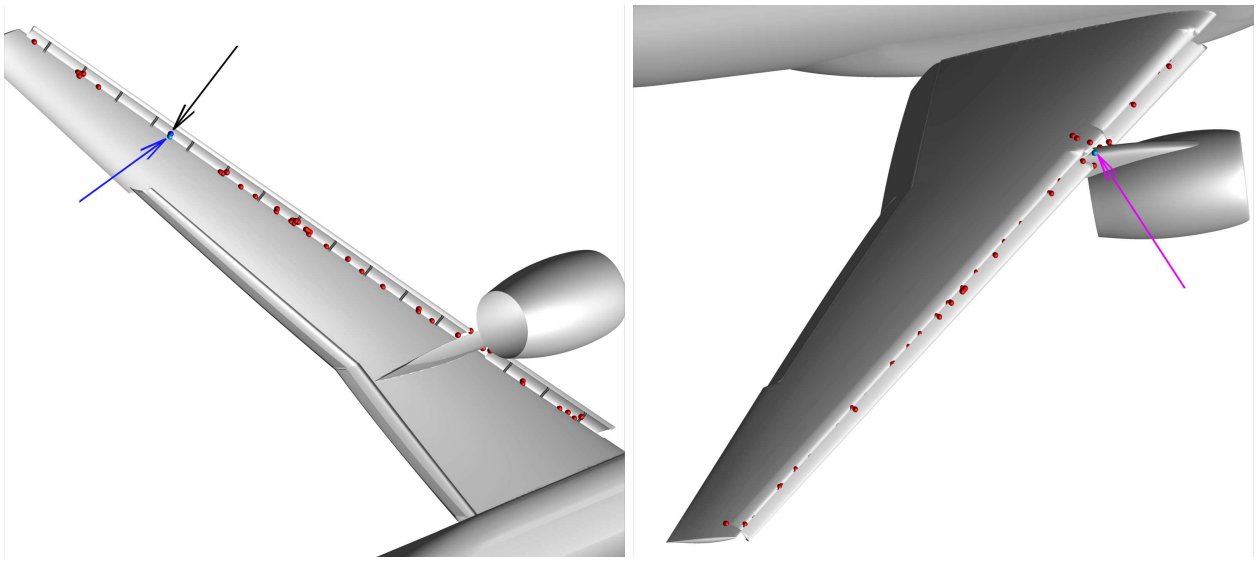

Fig. 9 Images of the CRM-HL showing the locations of unsteady pressure transducers as spheres.

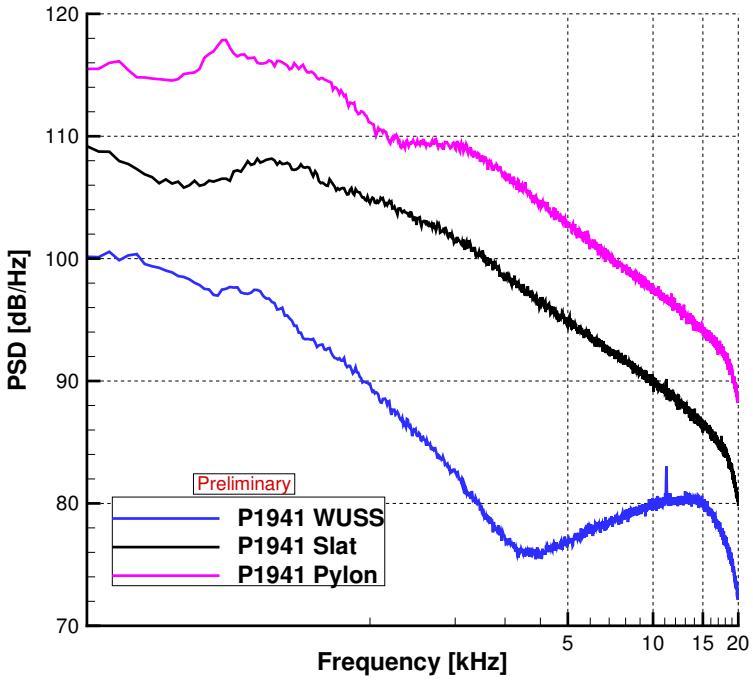

Fig. 10 Unsteady surface pressure transducer spectra for the PSS CRM-HL at an AoA of 8.5° and Mach 0.2. The colored lines in Fig 9 indicate the locations of the transducers.

Fig. 11 Photo of the microphone array at 70. The 90° position is directly below the model, inline with the center of the balance. Approximate array positions are also indicated.

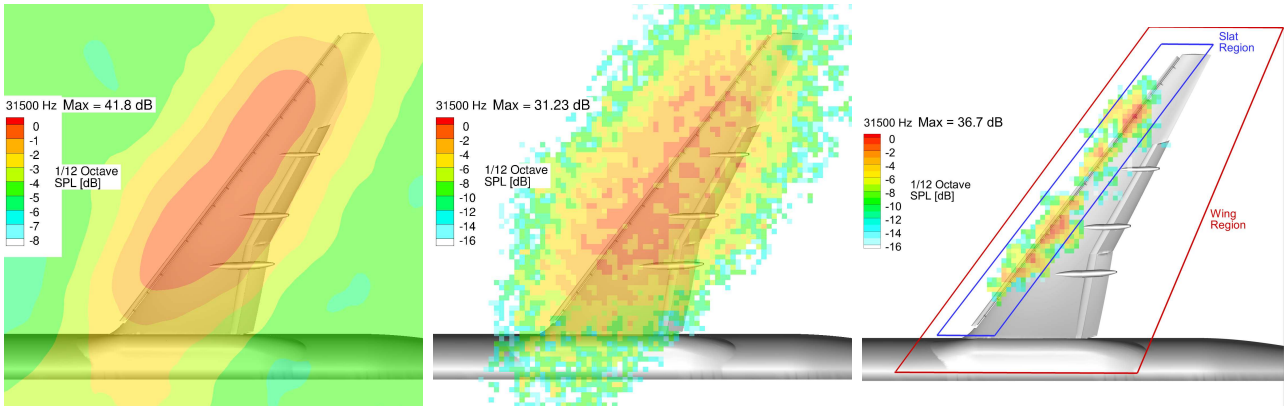

(a) Conventional (b) Traditional DAMAS (c) Coherence-Corrected DAMAS

Fig. 12 Beamforming output at the 31.5 kHz 1/12th-octave band for the CRM-HL model with the baseline FSS. Data are shown for the model at an AoA of 8.5° and the tunnel operating at Mach 0.2. The array is at the 90° station.

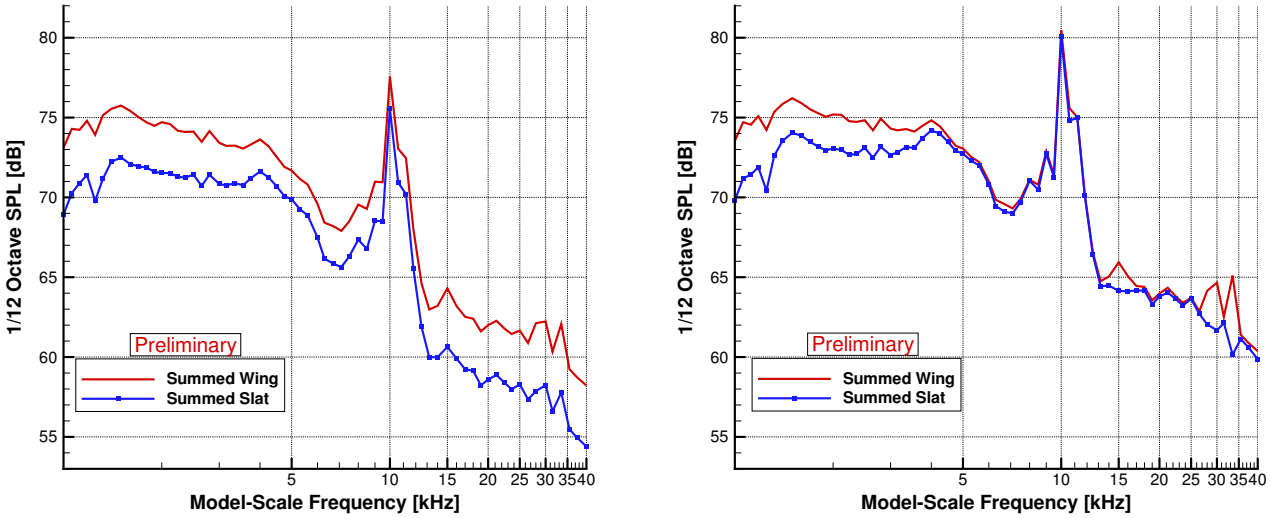

(a) Traditional DAMAS

(b) Coherence-Corrected DAMAS

Fig. 13 DAMAS output with summation bounds set for both the whole wing and isolated baseline full span slat. Data are shown for the CRM-HL model with the baseline FSS at an AoA of 8.5° and the tunnel operating at Mach 0.2. The array is at the 90° station.

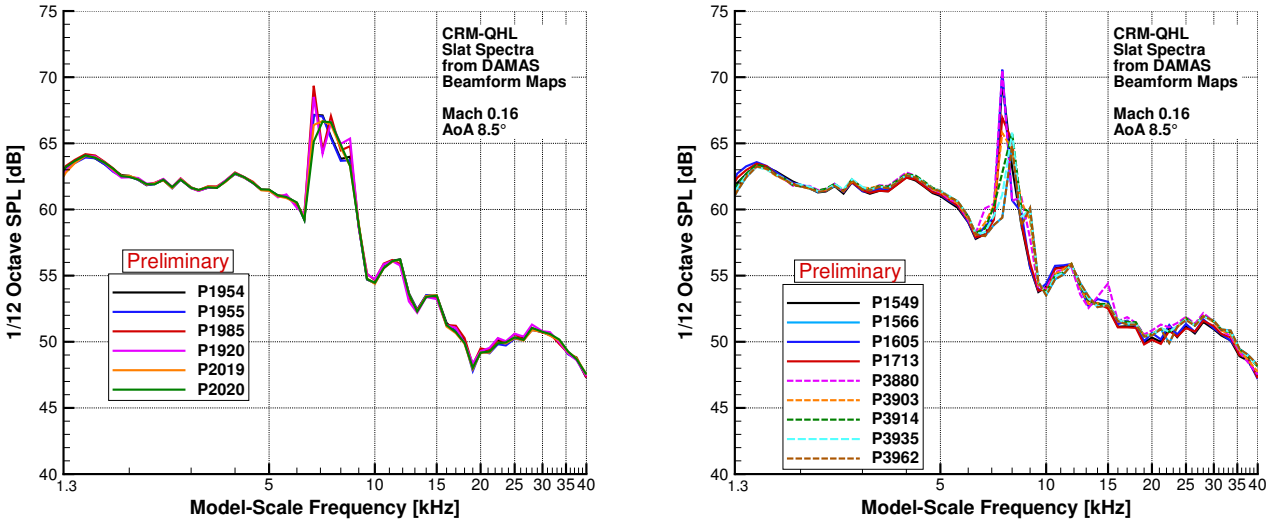

(a) PSS

(b) FSS

Fig. 14 DAMAS integrated spectra from the slat region for the baseline CRM-HL model at an AoA of 8.5° and Mach 0.16. The array is at the 90° station.

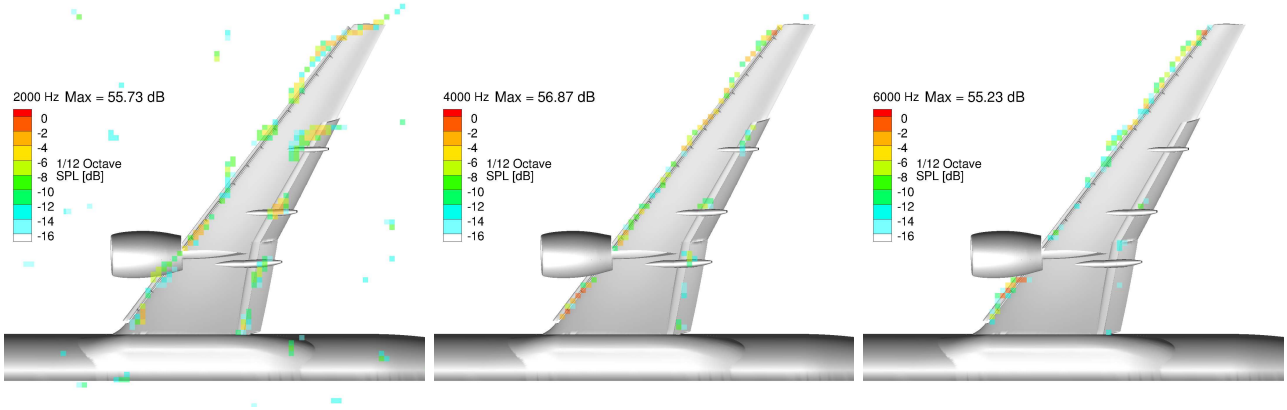

(a) 2 kHz (b) 4 kHz (c) 6 kHz

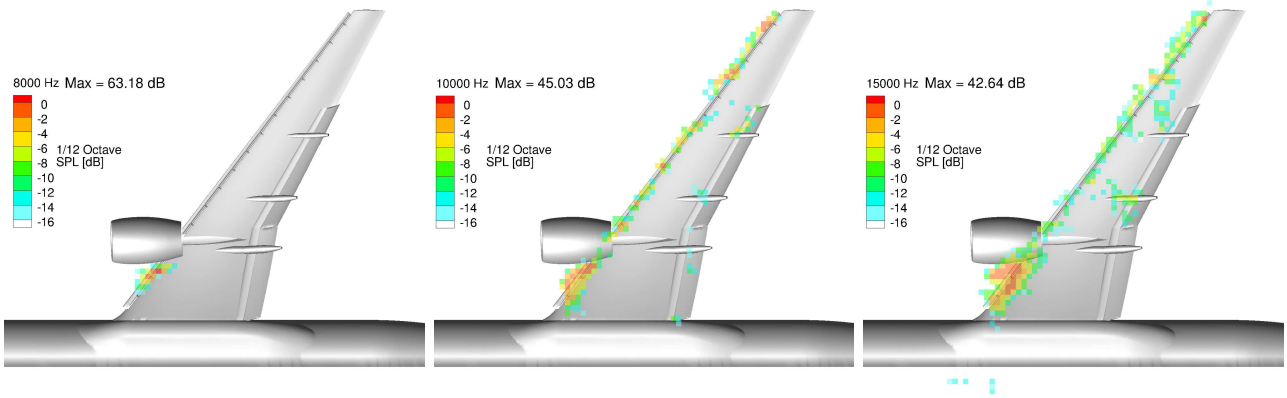

(d) 8 kHz (e) 10 kHz (f) 15 kHz

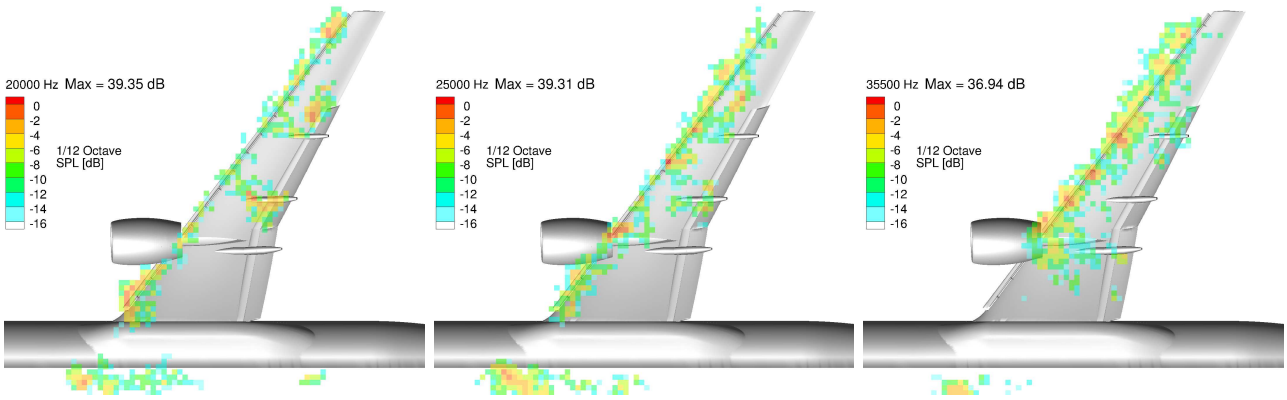

(g) 20 kHz (h) 25 kHz (i) 35 kHz

Fig. 15 Coherence-corrected 1/12th-octave DAMAS beamforming output for the PSS CRM-HL, P1920, AoA 8.5°, Mach 0.16, array at 90°.

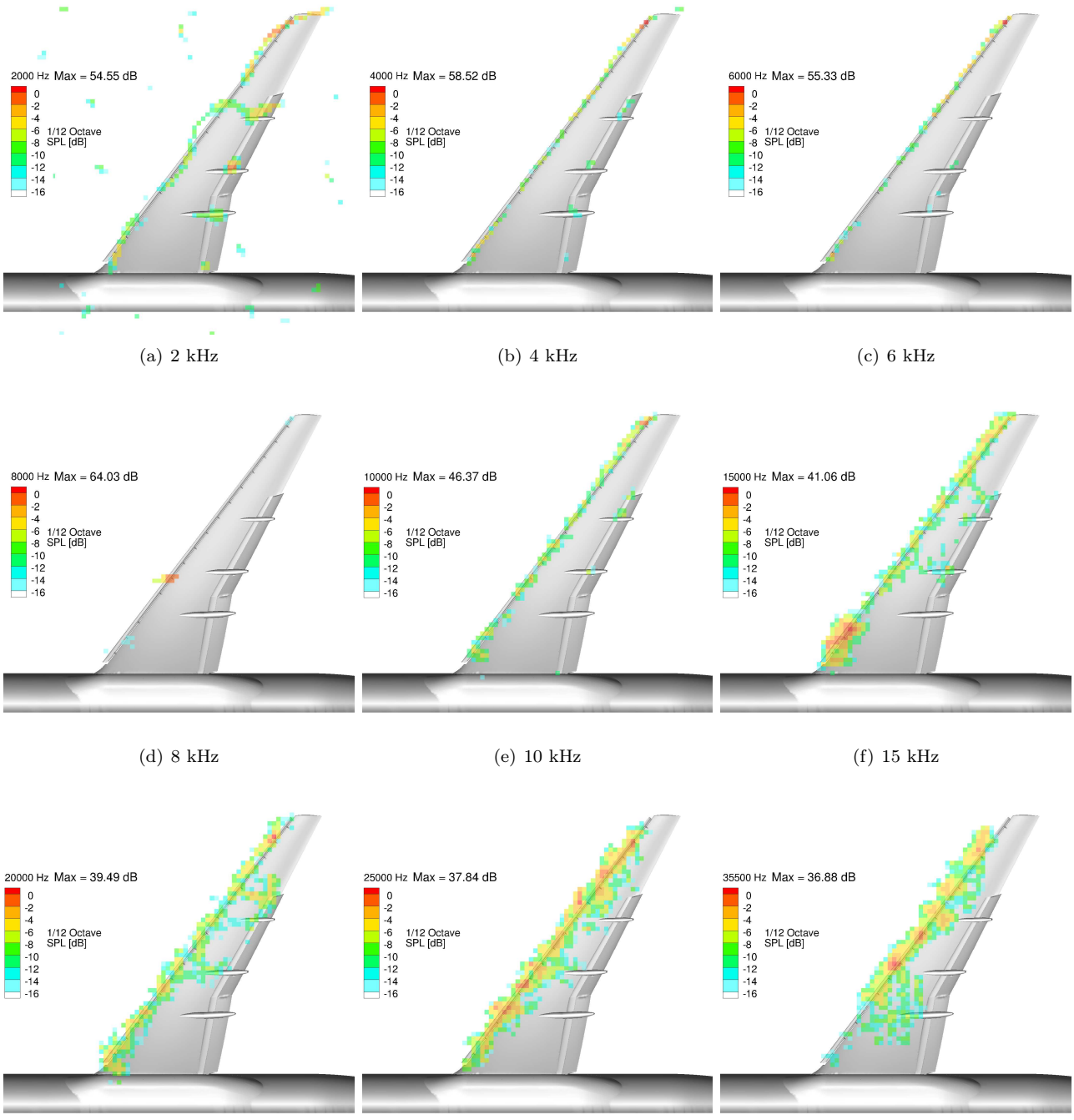

(a) 2 kHz (b) 4 kHz (c) 6 kHz

(d) 8 kHz (e) 10 kHz (f) 15 kHz

(g) 20 kHz (h) 25 kHz (i) 35 kHz

Fig. 16 Coherence-corrected 1/12th-octave DAMAS beamforming output for the FSS CRM-HL, P3914, AoA 8.5°, Mach 0.16, array at 90°.

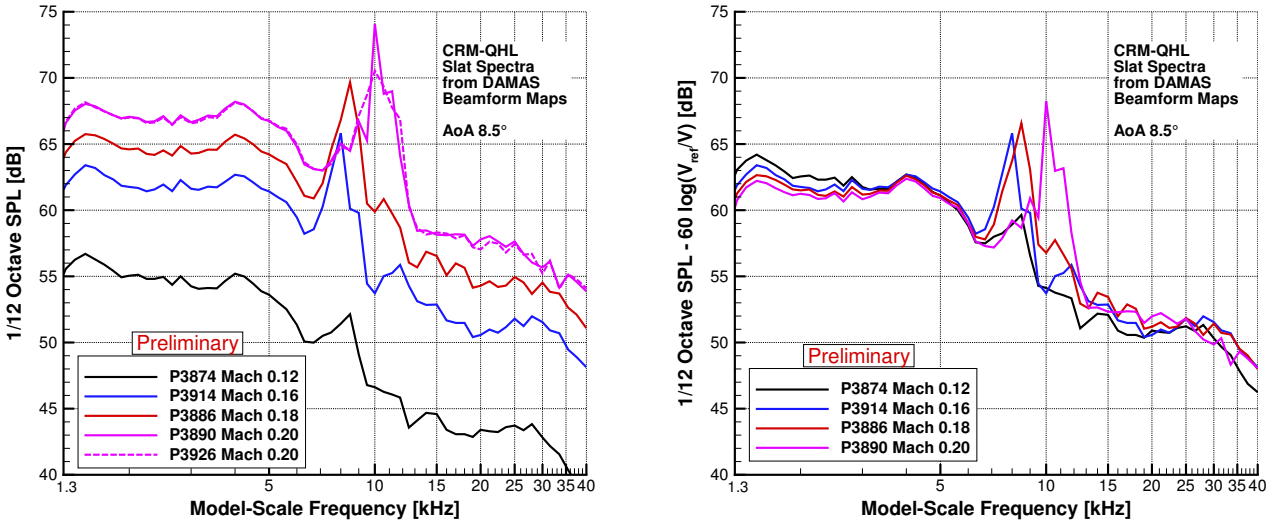

(a) Unscaled

(b) Scaled with V^6

Fig. 17 DAMAS slat region integrated spectra for the FSS CRM-HL model at an AoA of 8.5° showing the effect of Mach number. The array is at the 90° station.

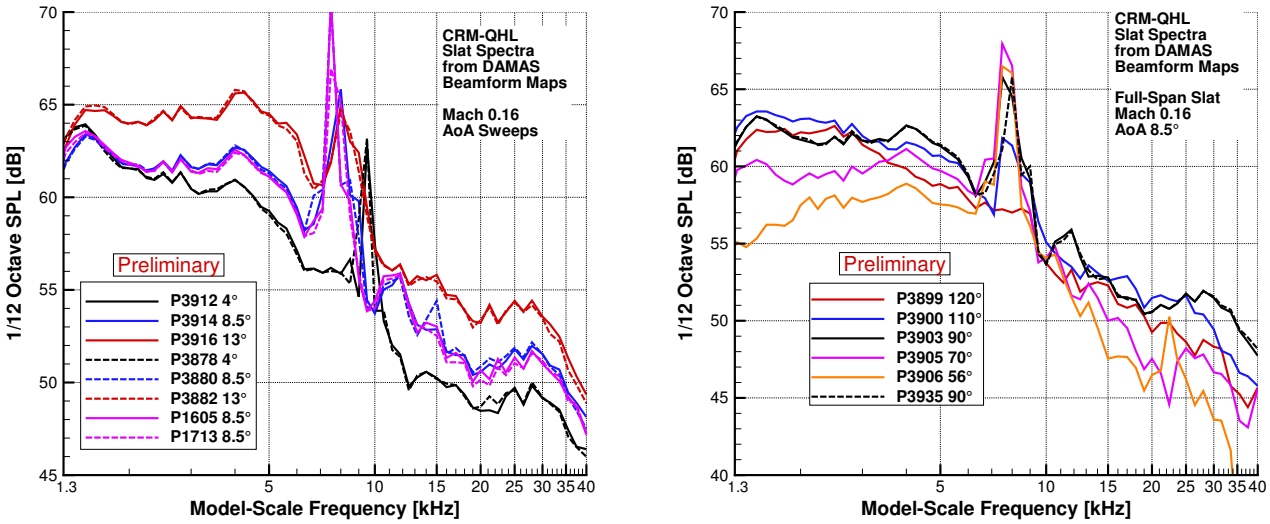

(a) AoA Variation at 90°

(b) Array Traverse

Fig. 18 DAMAS slat region integrated spectra for the FSS CRM-HL model, Mach 0.16, showing the effect of array position and AoA.

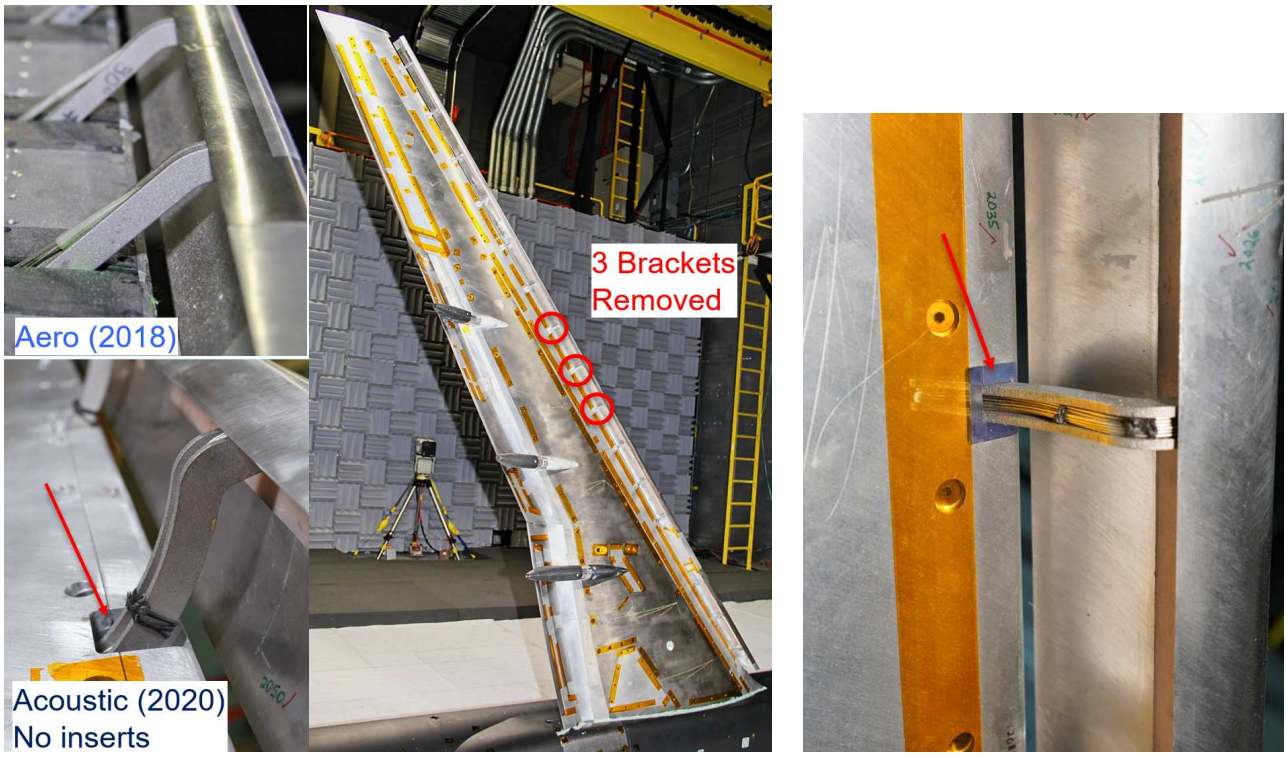

(a) Slat Brackets (b) Bracket Inserts

Fig. 19 Images of the CRM-HL Model showing slat bracket detail.

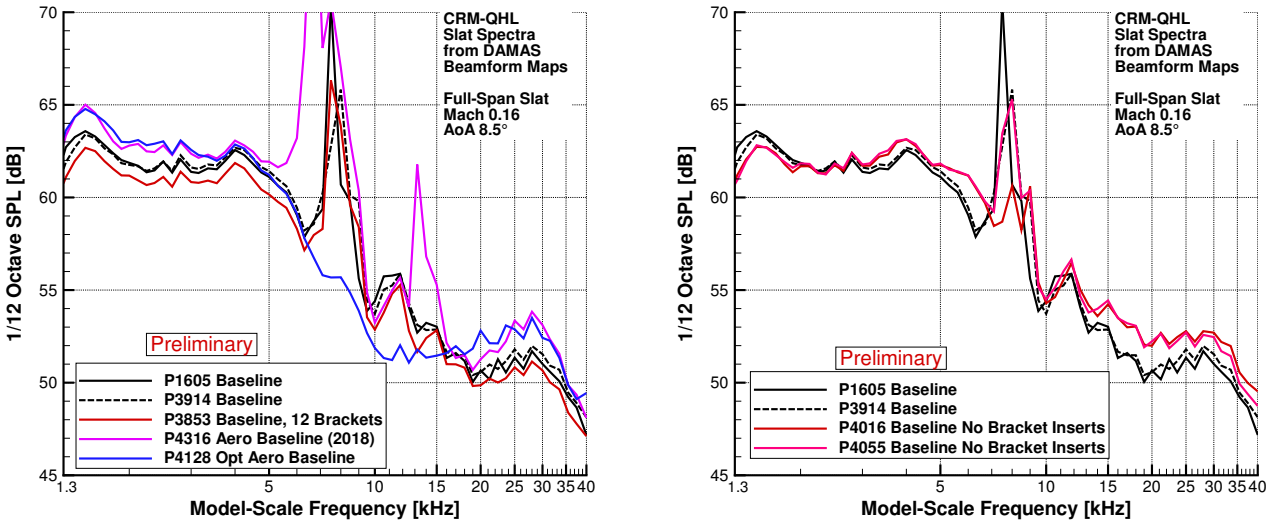

(a) Effect of Gaps, Brackets (b) Effect of Bracket Inserts

Fig. 20 DAMAS slat region integrated spectra for the FSS CRM-HL model at an AoA 8.5°, Mach 0.16, array at 90° showing effect of gaps, brackets, and bracket inserts.

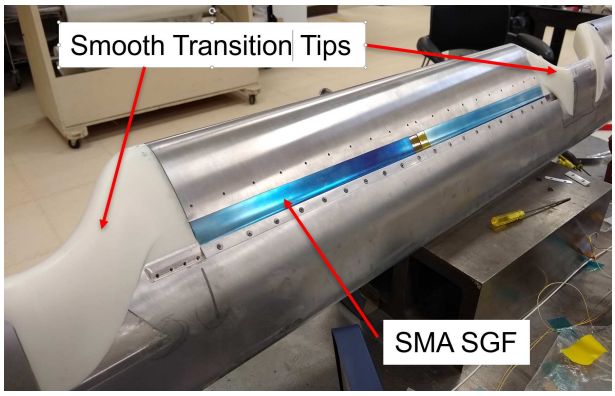

(a) SGF with Smooth Tips

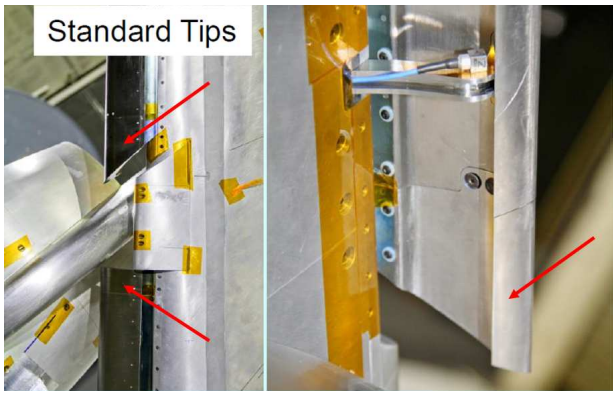

(b) SGF with Standard Tips

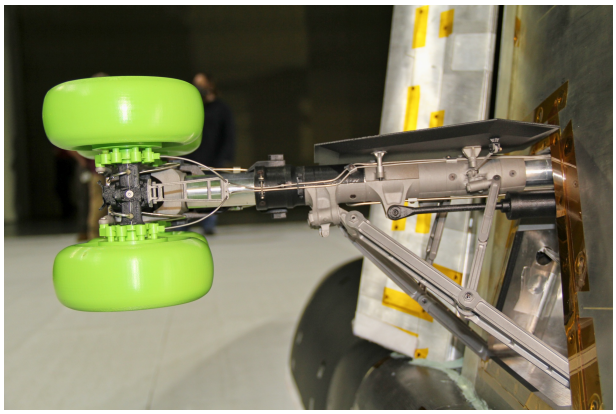

(c) MLG

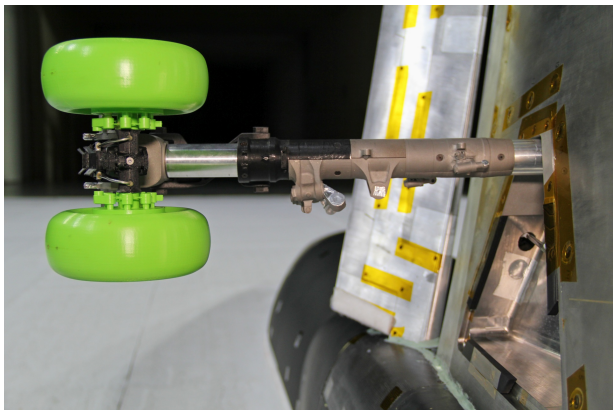

(d) Simple MLG

Fig. 21 Images of the CRM-HL Model showing slat treatment and landing gear details.

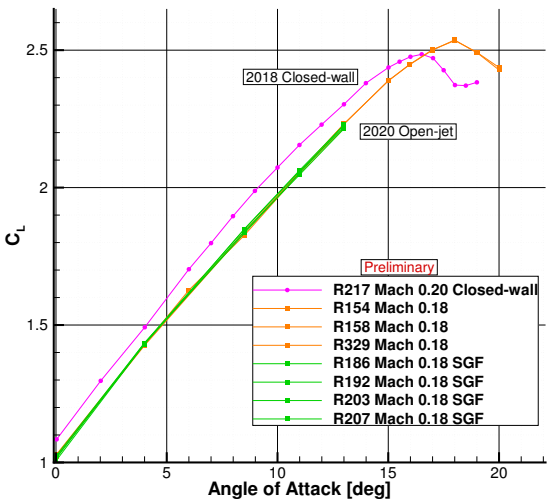

(a) Lift

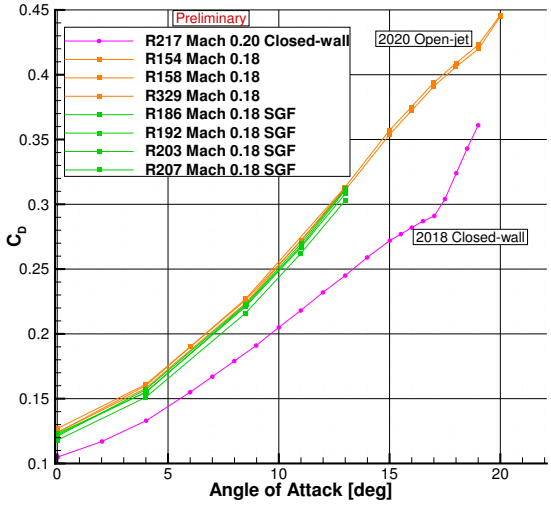

(b) Drag

Fig. 22 Lift and drag of the CRM-HL with the SGF installed on the PSS.

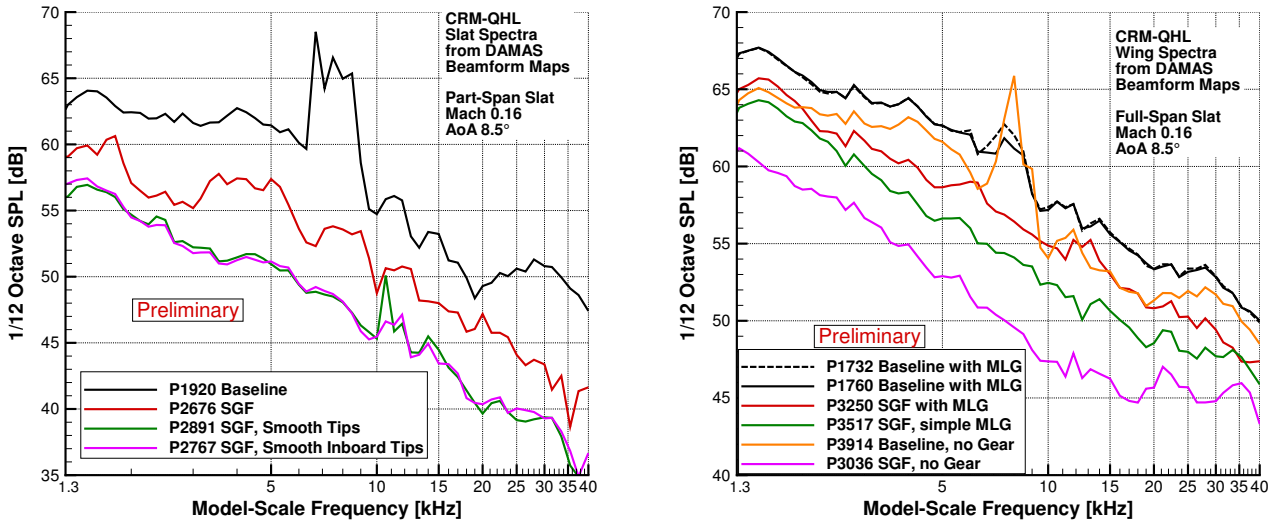

(a) PSS, Slat Region

(b) FSS, Wing Region

Fig. 23 DAMAS integrated spectra for the CRM-HL model at an AoA 8.5°, Mach 0.16, array at 90°.

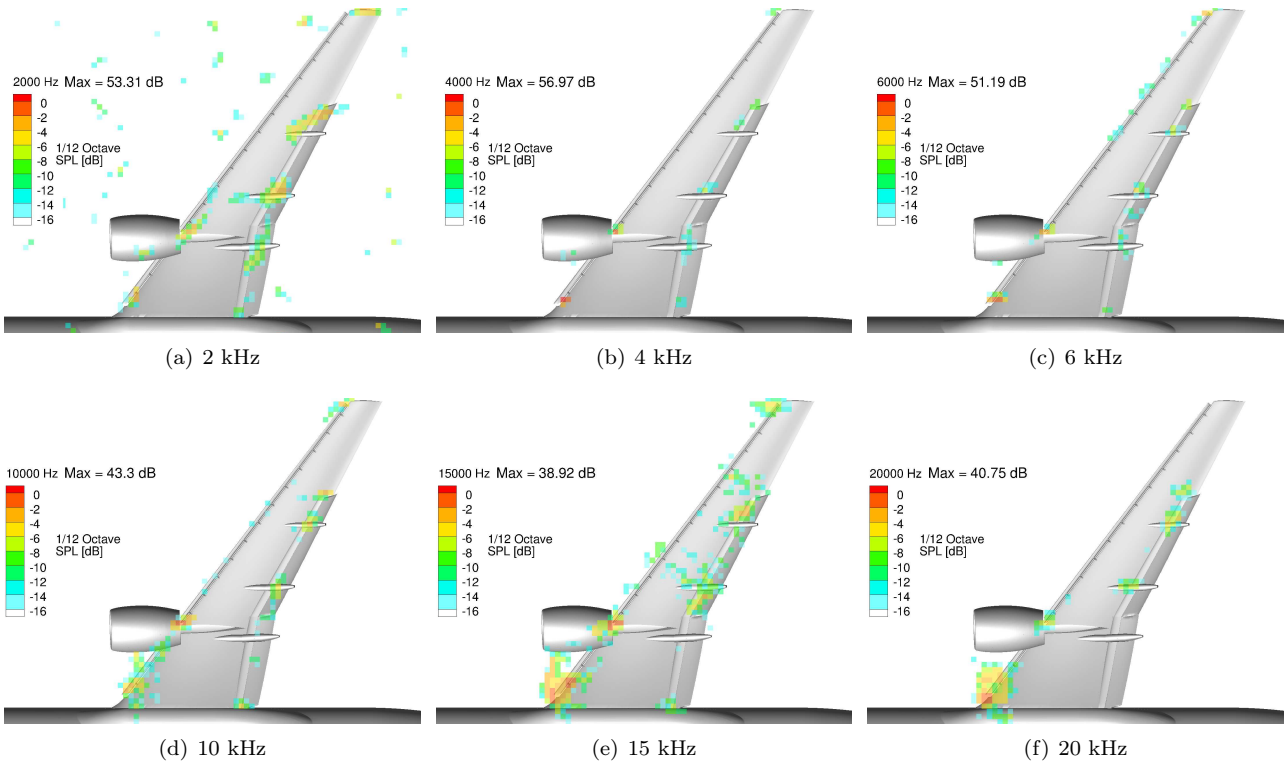

(a) 2 kHz

(b) 4 kHz

(c) 6 kHz

(d) 10 kHz

(e) 15 kHz

(f) 20 kHz

Fig. 24 Coherence-corrected 1/12th-octave DAMAS beamforming output for the PSS SGF CRM-HL with standard tips, P2676, AoA 8.5°, Mach 0.16, array at 90°.

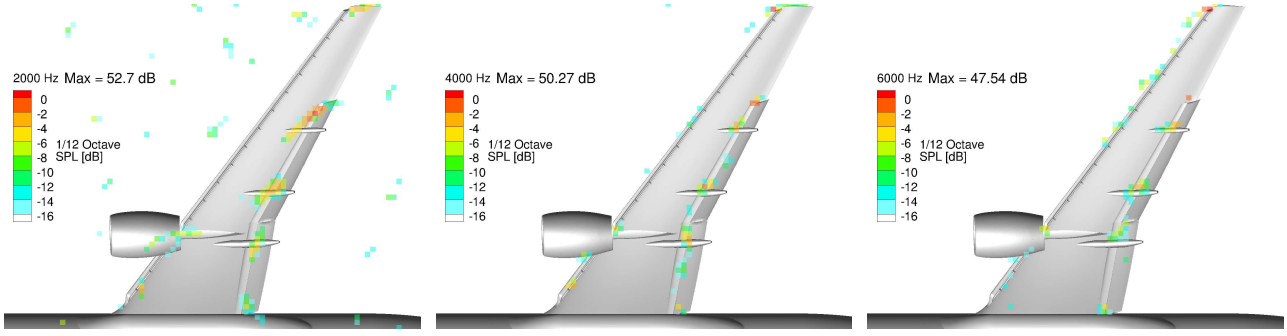

(a) 2 kHz (b) 4 kHz (c) 6 kHz

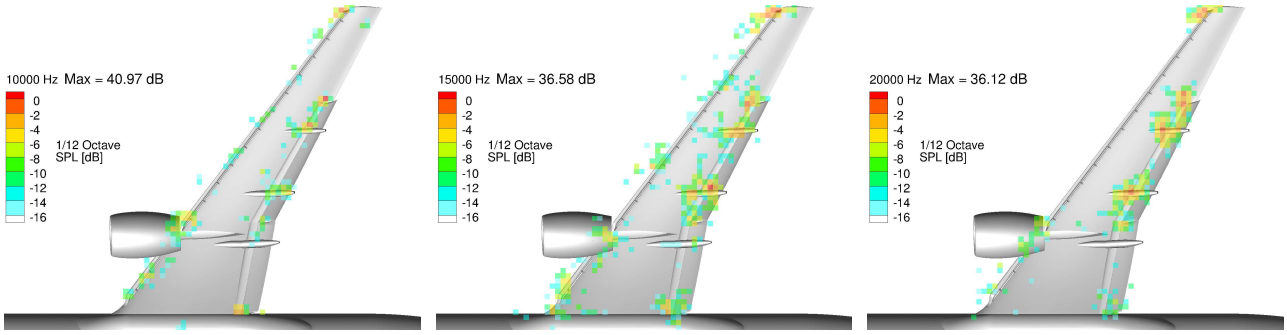

(d) 10 kHz (e) 15 kHz (f) 20 kHz

Fig. 25 Coherence-corrected 1/12th-octave DAMAS beamforming output for the PSS SGF CRM-HL with smooth tips, P2767, AoA 8.5°, Mach 0.16, array at 90°.

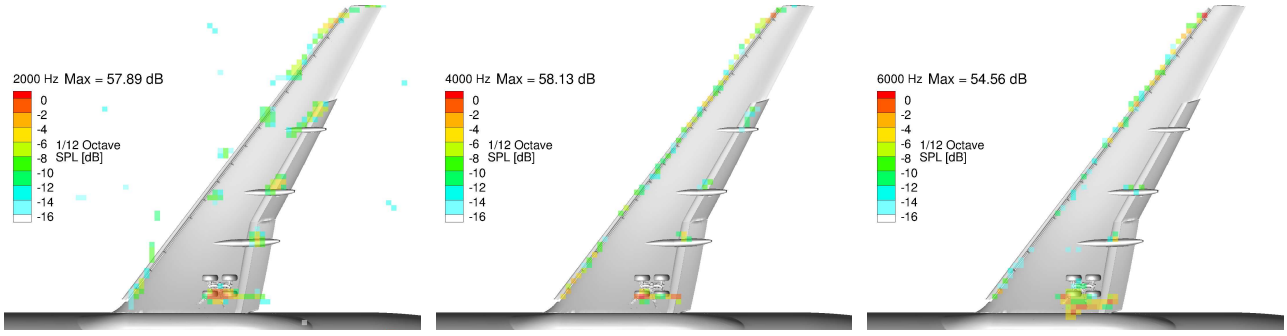

(a) 2 kHz (b) 4 kHz (c) 6 kHz

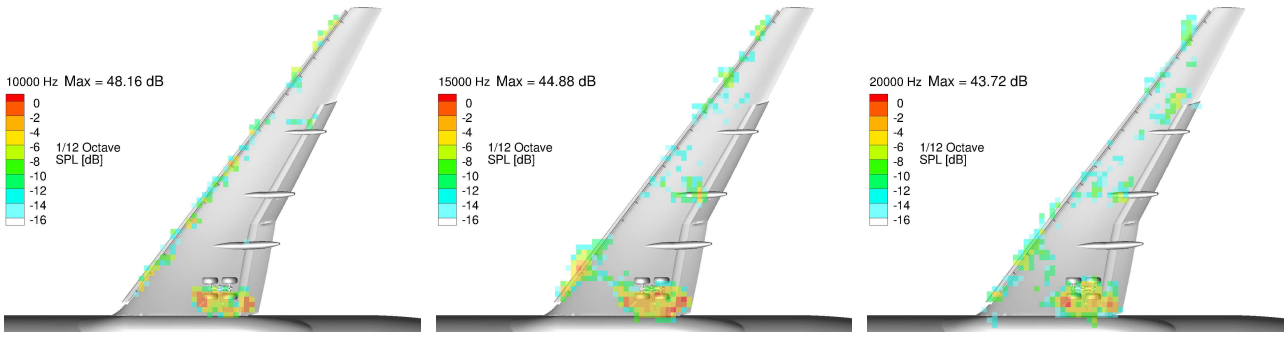

(d) 10 kHz (e) 15 kHz (f) 20 kHz

Fig. 26 Coherence-corrected 1/12th-octave DAMAS beamforming output for the FSS CRM-HL with MLG, P1760, AoA 8.5°, Mach 0.16, array at 90°.

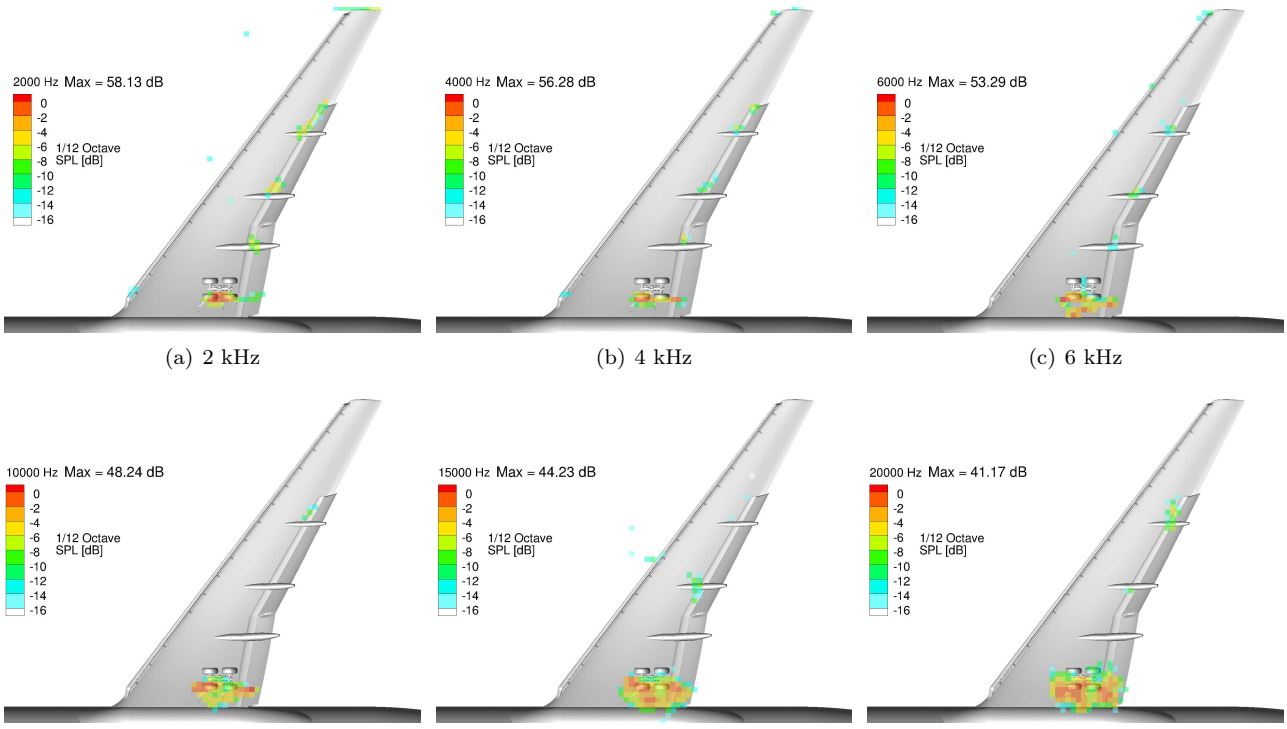

(a) 2 kHz (b) 4 kHz (c) 6 kHz

(d) 10 kHz (e) 15 kHz (f) 20 kHz

Fig. 27 Coherence-corrected 1/12th-octave DAMAS beamforming output for the FSS SGF CRM-HL with MLG, P3250, AoA 8.5°, Mach 0.16, array at 90°.